Emergence of Chirality from Isotropic Interactions of Three Length Scales

S. K. Mkhonta, K. R. Elder, and Zhi-Feng Huang

Phys. Rev. Lett. **116**, 205502 — Published 18 May 2016

DOI: 10.1103/PhysRevLett.116.205502

Emergence of Chirality from Isotropic Interactions of Three Length Scales

S. K. Mkhonta,[1,2] K. R. Elder,[3] and Zhi-Feng Huang[1]

[1] *Department of Physics and Astronomy, Wayne State University, Detroit, Michigan 48201, USA*
[2] *Department of Physics, University of Swaziland, Private Bag 4, Kwaluseni, Swaziland*
[3] *Department of Physics, Oakland University, Rochester, Michigan 48309, USA*

(Dated: April 26, 2016)

Chirality is known to play a pivotal role in determining material properties and functionalities. However, it remains a great challenge to understand and control the emergence of chirality and the related enantioselective process particularly when the building components of the system are achiral. Here we explore the generic mechanisms driving the formation of two-dimensional chiral structures in systems characterized by isotropic interactions and three competing length scales. We demonstrate that starting from isotropic and rotationally invariant interactions, a variety of chiral ordered patterns and superlattices with anisotropic but achiral units can self-assemble. The mechanisms for selecting specific states are related to the length-scale coupling and the selection of resonant density wave vectors. Sample phase diagrams and chiral elastic properties are identified. These findings provide a viable route for predicting chiral phases and selecting the desired handedness.

PACS numbers: 81.16.Dn, 61.50.Ah, 81.10.Aj, 81.16.Rf

Chirality is a fundamental characteristic that has profound implications in science. Its emergence is largely governed by the interplay of geometry, interactions, and surface functionality of the system building blocks. While it is natural to expect chirality in systems with chiral components (e.g., single-handed biochemical molecules) and specific anisotropic interactions, interestingly chirality can also emerge in systems composed of achiral building blocks. This has been observed in recent experiments on colloids (e.g., the controlled self-assembly of colloidal helical chains under magnetic field [1] and planar chiral patterns with long range order [2–4]), self-assembling faceted nanocrystals [5], and inorganic-organic hybrid materials that are of significant potential in biochemical and pharmaceutical applications [6].

Although a considerable amount of effort has been devoted to understanding these phenomena, most of the existing theoretical studies are based on atomistic simulations (Monte Carlo or molecular dynamics) using predetermined and tailored interparticle potentials. These have been applied to the investigations of self-assembly processes [7–14], in particular for systems governed by isotropic interactions [7–12] which can even lead to chiral patterns [9]. These results are dependent on atomistic details such as the type and shape of individual constituents and the form of their mutual interactions that vary vastly between systems. It is thus important to identify the underlying generic mechanisms that give rise to these fascinating findings.

One of the key factors controlling the ordering process is the coupling among different length scales. Recent studies have demonstrated that up to three length scales are sufficient to produce all five two-dimensional (2D) Bravais lattices and other ordered phases [15], while interparticle interactions of two length scales can lead to 6 different 2D quasicrystalline orders [11]. One would expect this length-scale factor also plays an important role on the emergence of system chirality. Chirality in 2D patterns is characterized by the lack of symmetry axes, and that the mirror image of a chiral pattern cannot be translated and rotated to coincide with itself. Such chiral patterns can simply emerge from the interference of plane waves with unequal wavelengths, representing different length scales of the system (see Fig. S1 of the supplemental material [16]). The length-scale effect can also be inferred from recent experiments where chirality emerges in colloidal or nanocrystal systems composed of achiral shaped particles such as rhombs [3], square crosses [4], nano-octapods [2], and elongated hexagons [5]. These geometries of building blocks give rise to various effective length scales of interparticle couplings and interactions.

Here we provide a comprehensive study of 2D chiral pattern selection, using a modeling method based on basic arguments of symmetry and length scales. We examine how chirality arises from isotropic interactions in systems with underlying achiral base symmetries. Via controlling three competing length scales we identify and predict various chiral phases and superlattices and determine the elastic properties. Although the building blocks of the patterns display different shapes and types, a scenario similar to that found in experiments and atomistic simulations, we show that the basic selection mechanisms are generic and depend only on the nonlinear coupling and selection of system characteristic density waves.

The study here is based on the phase field crystal (PFC) method which has been applied to a wide range of solid and soft matter systems across different scales [22–29]. We use a multimode PFC model that was developed very recently [15], with a free energy functional

$$\mathcal{F} = \int d\mathbf{r}\Big\{\lambda\psi\prod_{i=1}^{N}\left[\left(Q_i^2+\nabla^2\right)^2+b_i\right]\psi/2 + r\psi^2/2 - \tau\psi^3/3+\psi^4/4\Big\}, \quad (1)$$

and the dissipative or diffusive dynamics for the atomic density field ψ, i.e., $\partial\psi/\partial t = -(-\nabla^2)^n \delta\mathcal{F}/\delta\psi$ (with $n = 0$ or 1). This model incorporates the coupling and competition between multiple length scales (i.e., N Q_i modes) in a simple and fundamental way. Here λ is related to the system elastic constants, and b_i gives the relative weight of each excited density mode. The parameter r controls the transition between a homogeneous state (with constant ψ) and an ordered state (with ψ varying periodically). It is proportional to the distance from the melting temperature during crystallization [16], or in isothermal colloidal or nanocrystal self-assembled systems, it is determined by the attraction strength between constituent particles [30] (with larger $|r|$ corresponding to larger strength, as controlled e.g., by tuning the solvent of colloidal suspension [31]). In the following we examine both ranges of small and large $|r|$ values, corresponding to weak and strong segregation regimes of structural ordering. In addition, the coefficient τ of the cubic term in Eq. (1) is proportional to the strength of three-point correlation and can be derived from classical dynamic density functional theory [24].

The free energy functional in Eq. (1) is rotationally invariant, and can be used to construct and design interparticle pair potentials [10, 32] that are important for connecting with and designing experimental systems as conducted previously via atomistic simulations [5, 31]. Details are given in the supplemental material [16], which also discusses the isotropic nature of the pair interaction potential in multimode PFC and the importance of the relative magnitude of the wave numbers Q_i in determining the base symmetry of the selected periodic states.

To examine the ordered states we expand $\psi(\mathbf{r}) = \psi_0 + \sum_{\mathbf{q}} a_{\mathbf{q}} e^{i(\mathbf{q}\cdot\mathbf{r}+\phi_{\mathbf{q}})}$, where $a_{\mathbf{q}}$ are real amplitudes, $\mathbf{q}$ is the wave vector, $\phi_{\mathbf{q}}$ is the phase and ψ_0 the average density. From Eq. (1) the free energy density ($f = \mathcal{F}/\text{area}$) is given by

$$
\begin{aligned}
f = &\sum_{\mathbf{q}} G(q) a_{\mathbf{q}}^2 \\
&+\frac{w}{3} \sum_{\mathbf{q}_1\mathbf{q}_2\mathbf{q}_3} a_{\mathbf{q}_1} a_{\mathbf{q}_2} a_{\mathbf{q}_3} \cos\left(\sum_{i=1}^{3} \phi_{\mathbf{q}_i}\right) \delta_{\mathbf{q}_1+\mathbf{q}_2+\mathbf{q}_3,0} \qquad (2) \\
&+\frac{1}{4} \sum_{\mathbf{q}_1\mathbf{q}_2\mathbf{q}_3\mathbf{q}_4} a_{\mathbf{q}_1} a_{\mathbf{q}_2} a_{\mathbf{q}_3} a_{\mathbf{q}_4} \cos\left(\sum_{i=1}^{4} \phi_{\mathbf{q}_i}\right) \delta_{\mathbf{q}_1+\mathbf{q}_2+\mathbf{q}_3+\mathbf{q}_4,0},
\end{aligned}
$$

where $w = 3\psi_0 - \tau$ and $G(q) = \{r + \lambda \prod_{i=1}^{N} [(Q_i^2 - q^2)^2 + b_i]\}/2 - \tau\psi_0 + 3\psi_0^2/2$. The parameter w determines the relative weight of cubic coupling with respect to the quartic one, and plays an important role in controlling the intrinsic symmetry of the pattern. Two fundamentally different types of symmetry, corresponding to $w = 0$ vs $w \neq 0$, will be studied below.

Close to the ordering transition the amplitudes $a_{\mathbf{q}}$ are small and the cubic energy term dominates [33]. This term couples 3 waves with a resonant condition $\mathbf{q}_1 + \mathbf{q}_2 + \mathbf{q}_3 = 0$ and can always reduce the system free energy with a negative contribution. From a geometric perspective, a resonant triad of wave vectors forming a closed loop can form an equilateral, isosceles, scalene, or collinear triangle, and the following point group symmetries can be stabilized by the 3-waves coupling: C_6, C_4, D_2, and C_1. Which of them is preferred depends on the number and nature of the length scales involved [15]. For example, the chiral symmetry C_1 can emerge when $N = 3$, i.e., the wave-vector triplet forms a scalene triangle.

For systems further from the transition, the quartic coupling would play a larger role. It alone can also stabilize different symmetries provided at least two length scales are involved [34]. For example, exotic patterns and superlattices have been observed in shaken convective fluids with 4-waves resonance [35]. From Eq. (2), the quartic energy term is characterized by tetrads of density wave vectors satisfying the resonant condition $\sum_{i=1}^{4} \mathbf{q}_i = 0$. The basic combinations of wave vectors involve a set of 4 density waves with pairwise vectors $\{\pm\mathbf{q}_1, \pm\mathbf{q}_2\}$, giving a positive contribution to the free energy. There are also nontrivial couplings such as non-pairwise resonant tetrads $\mathbf{k}_1 + \mathbf{k}_2 + \mathbf{k}_3 + \mathbf{p} = 0$, $\mathbf{k}_1 + \mathbf{k}_2 + \mathbf{p}_1 + \mathbf{p}_2 = 0$, or $\mathbf{k}_1 + \mathbf{k}_2 + \mathbf{p} + \mathbf{s} = 0$ ($|\mathbf{k}| \neq |\mathbf{p}| \neq |\mathbf{s}|$; see supplemental Fig. S6 [16]). The related phase factors are nonzero and similar to the cubic term, this quartic coupling can provide a negative contribution to the free energy, leading to the formation of novel ordered and chiral phases.

Additionally, some chiral symmetries may emerge from the competition between these two nonlinear couplings. The cubic coupling may stabilize structures with a number of triads. However, such structures could pay a heavy quartic energy penalty since they would involve pairwise wave vectors $\{\pm\mathbf{q}\}$. Consequently, a chiral state with fewer number of density wave vectors forming an asymmetric set of non-pairwise tetrads may be favored at the expense of the more symmetric state. The precise number of positive and negative contributions that appear due to cubic and quartic couplings is summarized in supplemental Table S1 for several different symmetries [16].

We have conducted numerical simulations to verify the above analysis, starting from an initially homogeneous state with random fluctuations of $\psi_0 = 0$ and $N = 3$. For simplicity we assume that the density waves for different length scales are of the same excitation level, i.e., $b_i = 0$. This allows us to choose a sufficiently large range of λ (from 0.02 to 100), to tune the system elastic constants and address the chirality of both "soft" (with small λ) and "hard" crystals that are beyond the previous study [15]. The PFC dynamic equation was solved numerically via a pseudo-spectral algorithm [36] with periodic boundary conditions. Low-energy states were identified as steady-state solutions of the purely dissipative dynamics over a number of different random initial conditions.

We first investigate whether chiral structures may emerge from the quartic coupling alone, by setting $w = 0$.

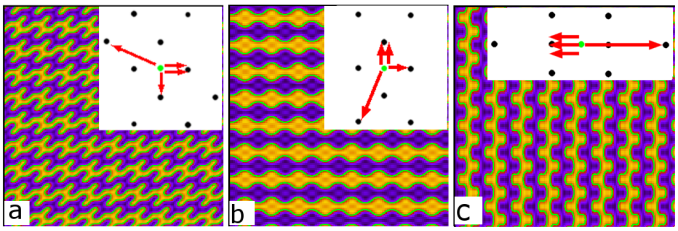

FIG. 1. Stripe superlattices (SSL) obtained from PFC simulations, for $w = 0$, $\lambda = 100$, and $Q_{1,2,3} = 1, 2, \sqrt{5}$ (a,b) or $1, \sqrt{2}, 3$ (c). (a) Chiral SSL at $r = -0.05$, with Frieze group $p211$. (b) Achiral SSL at $r = -0.15$, with Frieze group $p2mm$. (c) Achiral SSL at $r = -0.1$, with Frieze group $p2mg$. The lighter-colored regions correspond to larger values of the density field ψ. The diffraction patterns are shown in the insets.

In this limit the system has the up-down symmetry of $\psi(\mathbf{r}) \to -\psi(\mathbf{r})$. Fig. 1 shows some stripe superlattices (SSL) that emerge as low-energy stable states, corresponding to Frieze space groups $p211$ (chiral), $p2mm$, and $p2mg$. The chiral SSL appears when the system is in the weak segregation regime (i.e., small $|r|$). As expected, the characteristic wave vectors of these states contain non-pairwise resonant tetrads which lead to free energy reduction [16], as highlighted in Fig. 1.

When $w \neq 0$ the up-down symmetry of the pattern is broken, with some sample results shown in Fig. 2. Here the ratio of system length scales is chosen according to the symmetry of the base Bravais lattice. For example, a rectangular base lattice is obtained by setting $N = 3$ and $Q_{1,2,3} = 1, \mu, \sqrt{1+\mu^2}$ in Figs. 2(a), (b) and (d), while a square base lattice is set at $(1, \sqrt{2}, 2)$ in Fig. 2(c). The chirality that appears in Figs. 2(a) and 2(b) is due to the misalignment of the constituent particles from the lattice symmetry axes, although both the particle and the lattice (rectangular) are achiral. This is different from Fig. 2(c) where the chirality arises from the lattice itself (oblique). More complex scenarios can be obtained in the form of achiral superlattice, with alternating local orientation of the particles [Fig. 2(d)]. Interestingly, this superlattice resembles those observed experimentally in monolayers of elongated nanoplates (although with smaller periodicity) [5]. All these results illustrate the pattern anisotropies, while our simulations are based on the isotropic PFC model, indicating that the chiral or achiral self-assembly process is due to the selection mechanism of resonant wave vectors. As shown in Fig. 2, the diffraction patterns of chiral (achiral) states are asymmetric (symmetric) and consist of a number of resonant wave-vector triads and tetrads, implying the important role played by the interplay of cubic and quartic couplings.

To further investigate the conditions of chiral pattern self-assembly, we construct a sample stability diagram in the r–w space based on both analytic calculations (see supplemental material [16]) and numerical simulations. As shown in Fig. 3, for the rectangular base the following

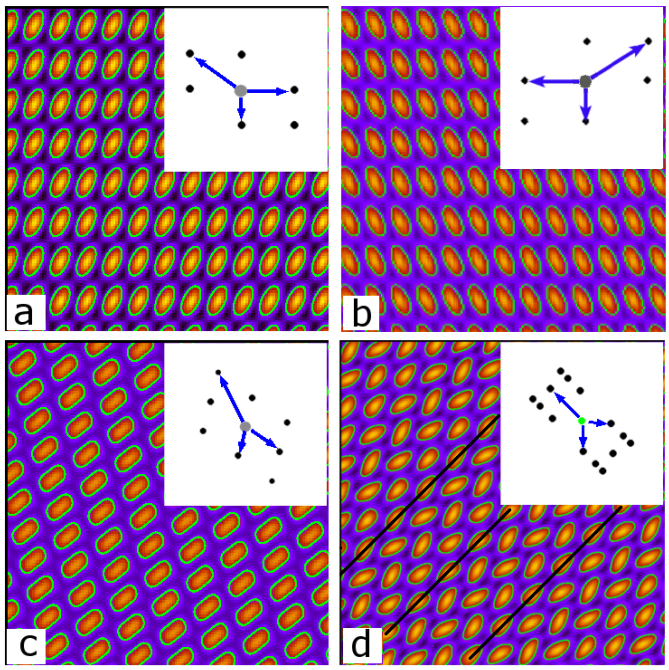

FIG. 2. Ordered phases and superlattices obtained from PFC simulations with $w = 1$, $\lambda = 100$, and $Q_{1,2,3} = 1, \mu, \sqrt{1+\mu^2}$ (a,b,d) or $1, \sqrt{2}, 2$ (c). (a) Right-handed and (b) left-handed chiral rectangular phases at $r = -1$ and $\mu = 3/2$. (c) Oblique phase at $r = -0.3$. (d) Achiral superlattice at $r = -1.5$ and $\mu = 1.35$, where solid lines indicate the axes of symmetry.

stable phases were obtained: rectangular, chiral rectangular, rectangular superlattice, stripe, and zigzag SSL. More results of phase diagrams in terms of r vs length scale ratio μ are given in supplemental Fig. S9. It is interesting to examine the transition between different states, particularly how a system with length scales that are commensurate with a symmetric achiral state can self-organize into a chiral state. For the example of rectangular state, the reciprocal vectors consist of a symmetric set of scalene-triangle loops (see Fig. 3). However, when w is decreased (i.e., weaker cubic coupling) the wave vector set becomes asymmetric with the reduction of triangle loops, resulting in two degenerate chiral states (left- and right-handed; see also Figs. 2(a) and 2(b)). This can be attributed to the corresponding energy contributions from the cubic vs quartic coupling, with details given in supplemental Table S1.

Our approach can be generalized to the study and prediction of a large variety of chiral or achiral structures through controlling the ratio of system length scales (i.e., Q_i). Some examples are given in Fig. 4, for soft vs rigid systems with $Q_{1,2,3} = 1, \sqrt{3}, \sqrt{7}$ yielding a triangular base lattice. For weak segregation and small elastic constants (small λ) the ordered state is achiral with a wallpaper symmetry group $p31m$ (see Fig. 4(a)). This soft crystal consists of cluster-like particles similar to those

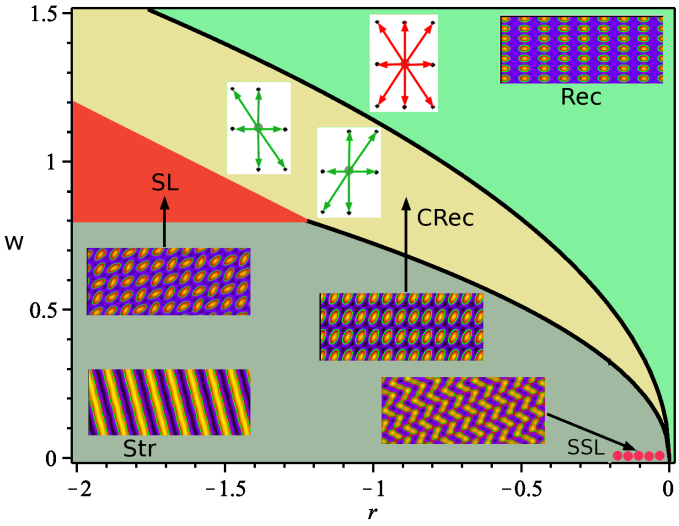

FIG. 3. Stability diagram for $Q_{1,2,3} = 1, \mu, \sqrt{1+\mu^2}$ with $\mu = 3/2$ and $\lambda = 100$, showing rectangular (Rec), chiral rectangular (CRec, with degenerate left- and right-handed states), rectangular superlattice (SL), chiral zigzag SSL, and stripe (Str) phases. The solid lines were obtained analytically from free energy calculations, while the shaded regions were identified from simulations.

observed in colloidal experiments [37] and MC simulations [7]. Further from the ordering transition threshold, for weaker cubic coupling (smaller w) and larger elastic constants (larger λ) these clusters are either stretched or connected, leading to chiral phases with an underlying triangular symmetry (see Figs. 4(b) and 4(c)). Similarly, the stability of these states can be attributed to the interplay between cubic and quartic nonlinear couplings. The achiral $p31m$ state is characterized by a symmetric set of wave vector triads (see Fig. 4(a) inset) and is therefore stabilized by the cubic energy term. However, for weaker cubic coupling such a symmetric combination of density modes causes a larger quartic energy penalty. This symmetry is then broken via reducing the number of wave vectors to form an asymmetric set containing non-pairwise resonant tetrads with negative quartic energy contribution and less number of triads (Figs. 4(b) and 4(c)), leading to the chiral phases.

It is interesting to identify the elastic properties of these chiral and achiral states. For example, a rectangular structure is characterized by 8 basic wave vectors: $\mathbf{q}_{1,2} = (\pm 1, 0)$, $\mathbf{q}_{3,4} = (0, \pm\mu)$, $\mathbf{q}_{5,6} = (\pm 1, \pm\mu)$, $\mathbf{q}_{7,8} = (\mp 1, \pm\mu)$, corresponding to 3 density modes of $Q_{1,2,3} = 1$, μ, $\sqrt{1+\mu^2}$ with amplitudes a_1, a_2, and a_3 respectively. Given a displacement vector $\mathbf{u}$ so that $\psi(\mathbf{r}) \to \psi(\mathbf{r}+\mathbf{u})$, in the small deformation limit we obtain the elastic energy density of the rectangular phase

$$E_{el} = \frac{1}{2}C_{11}u_{xx}^2 + \frac{1}{2}C_{22}u_{yy}^2 + C_{12}u_{xx}u_{yy} + 2C_{44}u_{xy}^2, \quad (3)$$

where $u_{ij} = (\partial_i u_j + \partial_j u_i)/2$ is the linear strain tensor.

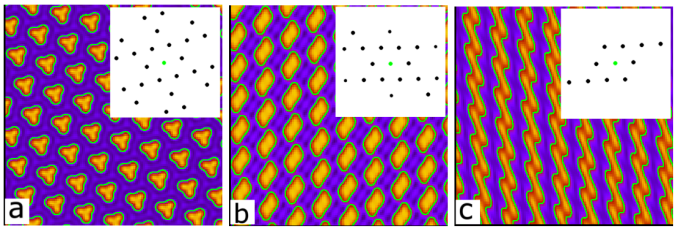

FIG. 4. Ordered phases for $Q_{1,2,3} = 1, \sqrt{3}, \sqrt{7}$ of triangular base. (a) Achiral phase with wallpaper plane group $p31m$, at $r = -0.05$, $\lambda = 0.02$, and $w = 2$. (b) Chiral phase with plane group $p2$, at $r = -1.7$, $\lambda = 10$, and $w = 1$. (c) Chiral stripelike state at $r = -2$, $\lambda = 10$, and $w = 1$.

The corresponding elastic constants are given by

$$C_{11} = 8\lambda\mu^4[a_1^2(1-\mu^2)^2 + 2a_3^2], \quad C_{12} = 16\lambda\mu^6 a_3^2,$$
$$C_{22} = 8\lambda\mu^4[a_2^2(1-\mu^2)^2 + 2a_3^2\mu^4], \quad C_{44} = C_{12}. \quad (4)$$

The chiral rectangular states are characterized by subsets of 6 wave vectors as shown in Fig. 3: $\{\mathbf{q}_{i=1,\ldots,6}\}$ and $\{\mathbf{q}_{i=1,\ldots,4}, \mathbf{q}_7, \mathbf{q}_8\}$ for right- and left-handed chirality. The elastic energy density of these two enantiomorphs is

$$E_{el} = \frac{1}{2}C_{11}u_{xx}^2 + \frac{1}{2}C_{22}u_{yy}^2 + C_{12}u_{xx}u_{yy} + 2C_{44}u_{xy}^2 + 2C_{14}u_{xx}u_{xy} + 2C_{24}u_{yy}u_{xy}, \quad (5)$$

where

$$C_{11} = 8\lambda\mu^4[a_1^2(1-\mu^2)^2 + a_3^2], \quad C_{12} = 8\lambda\mu^6 a_3^2,$$
$$C_{22} = 8\lambda\mu^4[a_2^2(1-\mu^2)^2 + a_3^2\mu^4], \quad C_{44} = C_{12},$$
$$C_{14} = \pm C_{12}/\mu, \quad C_{24} = \pm C_{12}\mu. \quad (6)$$

An important factor given in Eq. (6) is the chiral symmetry breaking revealed from two extra elastic constants C_{14} and C_{24}, the so-called chiral elastic constants for systems exhibiting chirality [38]. They are of positive or negative values in the right- or left-handed state respectively. This sign dependence would provide a viable way to identify and select the handedness of a chiral system elastically. For example, a simple shear can cause one enantiomorph to shrink and the other to expand, which would be of importance for the study of enantioselectivity and the control of homochirality with desired handedness as required in most applications [6].

In summary, our results have shown that systems with isotropic interactions and underlying achiral base symmetries can lead to surprisingly complex ordered and chiral states and that the formation and stabilization of 2D chiral structures are governed by two basic mechanisms: the selection of competing length scales that are commensurate to the symmetric base lattice, and the competition between cubic and quartic couplings that determines the characteristic density wave vectors of the pattern. As such our work should open up new avenues for more systematic investigations exploring the generic mechanisms

for the emergence of chirality in self-assembling systems. The approach developed here, which mostly relies on basic principles of symmetry and length scale competition, would provide a useful route for predicting and finding new and surprising chiral structures that possess novel properties. For example, the control of interaction length scales and wave vectors selection can be achieved either through tuning the interaction between building blocks or particles (via e.g., polymeric or DNA-functionalized colloidal nanoparticles) or effectively through selecting particle geometry, as is being actively pursued in experimental and theoretical studies of self assembly [5–14].

Z.-F.H. acknowledges support from the National Science Foundation (NSF) under Grant No. DMR-0845264. K.R.E. acknowledges support from the NSF under Grant No. DMR-1506634.

[1] D. Zerrouki, J. Baudry, D. Pine, P. Chaikin, and J. Bibette, Nature **455**, 380 (2008).
[2] W. Qi, J. de Graaf, F. Qiao, S. Marras, L. Manna, and M. Dijkstra, Nano Lett. **12**, 5299 (2012).
[3] K. Zhao and T. G. Mason, J. Am. Chem. Soc. **134**, 18125 (2012).
[4] K. Zhao and T. G. Mason, J. Phys. Condens. Matter **26**, 152101 (2014).
[5] X. Ye, J. Chen, M. Engel, J. A. Millan, W. Li, L. Qi, G. Xing, J. E. Collins, C. R. Kagan, J. Li, S. C. Glotzer, and C. B. Murray, Nat. Chem. **5**, 466 (2013).
[6] R. E. Morris and X. Bu, Nat. Chem. **2**, 353 (2010).
[7] M. Rechtsman, F. Stillinger, and S. Torquato, Phys. Rev. E **73**, 011406 (2006).
[8] B. M. Mladek, D. Gottwald, G. Kahl, M. Neumann, and C. N. Likos, Phys. Rev. Lett. **96**, 045701 (2006).
[9] E. Edlund, O. Lindgren, and M. N. Jacobi, Phys. Rev. Lett. **108**, 165502 (2012).
[10] K. Barkan, M. Engel, and R. Lifshitz, Phys. Rev. Lett. **113**, 098304 (2014).
[11] T. Dotera, T. Oshiro, and P. Ziherl, Nature **506**, 208 (2014).
[12] M. Engel, P. F. Damasceno, C. L. Phillips, and S. C. Glotzer, Nat. Mater. **14**, 109 (2015).
[13] S. P. Carmicheal and M. S. Shell, J. Chem. Phys. **139**, 164705 (2013).
[14] A. P. Gantapara, W. Qi, and M. Dijkstra, Soft Matter **11**, 8684 (2015).
[15] S. K. Mkhonta, K. R. Elder, and Z.-F. Huang, Phys. Rev. Lett. **111**, 035501 (2013).
[16] See Supplemental Material, which includes Refs. [17–21], for details of 2D chiral pattern description, isotropic interaction potentials, free energy expansion, and additional figures and phase diagrams.
[17] C. N. Likos, Phys. Rep. **348**, 267 (2001); A. A. Louis, P. G. Bolhuis, and J. P. Hansen, Phys. Rev. E **62**, 7961 (2000); C. N. Likos, A. Lang, M. Watzlawek, and H. Löwen, Phys. Rev. E **63**, 031206 (2001).
[18] J. A. Moriarty and M. Widom, Phys. Rev. B **56**, 7905 (1997).
[19] M. Mihalkovic and C. L. Henley, Phys. Rev. B **85**, 092102 (2012).
[20] G. Nägele, *The physics of colloidal soft matter* (Lecture Notes 14, Institute of Fundamental Technological Research, Polish academy of Science, Warsaw, 2004).
[21] L. Gronlund and N. D. Mermin, Phys. Rev. B **38**, 3699 (1988).
[22] K. R. Elder and M. Grant, Phys. Rev. E **70**, 051605 (2004).
[23] K. R. Elder, N. Provatas, J. Berry, P. Stefanovic, and M. Grant, Phys. Rev. B **75**, 064107 (2007).
[24] Z.-F. Huang, K. R. Elder, and N. Provatas, Phys. Rev. E **82**, 021605 (2010).
[25] H. Emmerich, H. Löwen, R. Wittkowski, T. Gruhn, G. I. Tóth, G. Tegze, and L. Gránásy, Adv. Phys. **61**, 665 (2012).
[26] A. Adland, Y. Xu, and A. Karma, Phys. Rev. Lett. **110**, 265504 (2013).
[27] E. J. Schwalbach, J. A. Warren, K.-A. Wu, and P. W. Voorhees, Phys. Rev. E **88**, 023306 (2013).
[28] A. M. Menzel, T. Ohta, and H. Löwen, Phys. Rev. E **89**, 022301 (2014).
[29] G. Kocher and N. Provatas, Phys. Rev. Lett. **114**, 155501 (2015).
[30] W. B. Russel, Phase Transitions **21**, 127 (1990).
[31] K. Miszta, J. de Graaf, G. Bertoni, D. Dorfs, R. Brescia, S. Marras, L. Ceseracciu, R. Cingolani, R. van Roij, M. Dijkstra, and L. Manna, Nat. Mater. **10**, 872 (2011).
[32] G. I. Tóth, T. Pusztai, G. Tegze, G. Tóth, and L. Gránásy, Phys. Rev. Lett. **107**, 175702 (2011).
[33] S. Alexander and J. McTague, Phys. Rev. Lett. **41**, 702 (1978).
[34] J. L. Jones and M. Olvera de la Cruz, J. Chem. Phys. **100**, 5272 (1994).
[35] J. L. Rogers, W. Pesch, O. Brausch, and M. F. Schatz, Phys. Rev. E **71**, 066214 (2005).
[36] M. Cheng and J. A. Warren, J. Comput. Phys. **227**, 6241 (2008).
[37] V. N. Manoharan, M. T. Elsesser, and D. J. Pine, Science **301**, 483 (2003).
[38] S. C. Cowin, *Continuum mechanics of anisotropic materials* (Springer, New York, 2013).